ACS Energy LETTERS

http://pubs.acs.org/journal/aelccp

Unveiling the Origin of Alloy-Seeded and Nondendritic Growth of Zn for Rechargeable Aqueous Zn Batteries

Yamin Zhang, Joshua D. Howe, Sarah Ben-Yoseph, Yutong Wu, and Nian Liu*

Cite This: *ACS Energy Lett.* 2021, 6, 404–412

Read Online

ACCESS | Metrics & More | Article Recommendations | Supporting Information

ABSTRACT: Rechargeable aqueous zinc anodes have gained tremendous attention because of their merits of intrinsic safety, low cost, and high theoretical volumetric capacity (5854 mAh cm^{-3} for Zn metal). In aqueous electrolytes, zinc anodes suffer from severe dendritic metal deposition. The regulation of Zn by inducing Zn-alloying metals has been reported. However, the underlying mechanisms have remained elusive. Here, for the first time, we did a comprehensive analysis to elucidate the mechanisms for the seeded and nondendritic growth of Zn on alloy anodes. We achieved uniform Zn deposition by introducing a Zn-alloying and soluble metal, Ag, on Zn anodes. Due to a shift of thermodynamic potential and the spatial confinement, the Ag-modified Zn anode exhibited improved overall cycling performance compared with previous deep-cycle Zn anodes. Furthermore, the seeded Zn deposition was visualized in operando for the first time using an optical microscope. The alloy-seeding design principle here can potentially be applied to improve the rechargeability of other metal anodes.

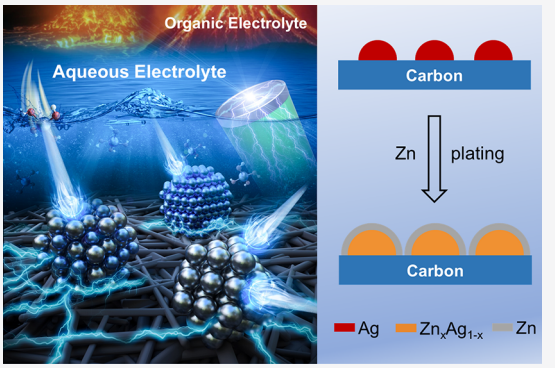

The current power-storage landscape is dominated by lithium-ion batteries (LIBs) because they provide high energy density and high rechargeability.[1,2] However, key elemental components for LIBs, such as Li and Co, will become much more costly to obtain in the near future. In addition, flammable organic electrolytes, which are used in LIBs, have raised numerous safety concerns.[3,4] As the size of a battery unit increases, the safety management of that unit poses additional challenges. Compared with batteries with flammable organic electrolytes, batteries with aqueous electrolytes, in which water is used as the solvent, generally feature better intrinsic safety, higher ionic conductivity and lower costs.[5−8] Among metals that are stable in water, zinc possesses the lowest redox potential (−0.762 V versus standard hydrogen electrode) and is therefore the most active metal anode compatible with aqueous electrolytes. Moreover, zinc has several other advantages, including a high theoretical capacity (820 mAh g^{-1}), high volumetric capacity (5854 versus 2062 mAh cm^{-3} for Li), low cost, and low toxicity.[9−13] These distinctive merits as well as new technologies that have been co-developed with LIBs, such as precise electrode material synthesis,[14] advanced accessory cell components,[15] and powerful diagnosis techniques,[16] have enabled a potential revival of zinc-based aqueous batteries.[17−20] Pairing zinc anodes with oxygen cathodes can yield Zn-air batteries,[21−25] which have prominent theoretical gravimetric and volumetric energy densities (1093 Wh kg^{-1} and 6134 Wh L^{-1}, respectively).

In aqueous electrolytes, zinc anodes suffer from severe nonuniform and dendritic metal deposition,[26,27] which results in the capacity decay over cycling. There are a few papers (summarized in Table S1) have reported that the addition of Au,[28] Ag,[29−35] Cu,[36−38] Al,[39] or In[40] on Zn anodes can effectively regulate Zn and improve the cycle life. On the basis of the success of adding these Zn-alloying metals, it is a key step toward high-performance Zn batteries to understand the mechanisms for the regulation of Zn and improvement, which have not been clearly elucidated yet.

Here, we report the mechanisms for the regulation of Zn on alloy anodes through comprehensive analysis for the first time. We discovered experimentally and computationally that in an alkaline electrolyte: (1) the Zn metal nucleation barrier substantially differs among different substrates, with some

Received: November 6, 2020
Accepted: December 28, 2020
Published: January 6, 2021

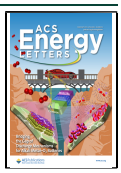

Zn-soluble materials showing zero potential barrier; (2) the formation of alloys between Zn and Zn-alloying materials is spontaneous during the electrochemical reduction of Zn(II), as a result of a negative Gibbs free energy of formation of zinc alloys. These discoveries suggest it feasible to nucleate and accommodate Zn metal. As a proof of concept, a spatially controlled and uniform Zn deposition through heterogeneous seeded growth has been achieved using Ag seeds. Notably, some past reports[28,29,38] have claimed seeded growth of Zn on Zn-alloying metals, however, which lacks evidence because seeded Zn deposition has not been clearly visualized. Here we visualized the seeded Zn deposition in operando for the first time using an optical microscope. The results of density functional theory suggest a more energetic Zn stripping process from Zn_xAg_{1-x} alloys and thus higher electrochemical potential of the Zn^{2+}/Zn_xAg_{1-x} redox than the Zn^{2+}/Zn redox, which can explain the anti-corrosion property of Zn alloy phases reported recently.[29,38−40] When the molar ratio between deposited Zn and Ag was controlled at 1, 2, and 3, the resultant Ag-nanoparticle-loaded carbon paper (C-Ag) achieved superior cycle lives of 75 187, 2501, and 752 cycles, respectively, compared with 273, 33, and 38 cycles for C electrodes, respectively. In addition, the Ag-modified Zn anode exhibits superior overall cycling performance compared with previously reported deeply cycled Zn anodes in alkaline electrolytes.

Choice of Seed Materials. We screened seven common metallic substrates (Ag, Au, Cu, Ti, Fe, Pt and Ni) that can potentially alloy with Zn. These substrates were prepared by evaporating the corresponding metal to a thickness of 100 nm onto Cu foils. The corresponding binary phase diagrams[41] are shown in Figures 1a and S1. The solubility zone is labeled as (Zn). Carbon-fiber paper, which does not alloy with or dissolve in zinc,[41] was also added in the above series as a control sample. We constructed a three-electrode electrochemical cell that consisted of the substrate of interest as the working electrode, Hg/HgO as the reference electrode and Zn foil as the counter electrode. Zn metal was galvanostatically deposited onto the working electrode at 3 mA cm^{-2} in an alkaline electrolyte (ZnO-saturated[42] 4 M KOH aqueous solution).

Figure 1b shows the voltage profiles of Zn metal deposition onto various substrates (Ag, Au, Cu, Ti, carbon). The Zn metal nucleation barrier is defined as the difference between the initial voltage dip and the later part of the voltage plateau, which is related to the miscibility of these materials with Zn.[43] Some materials have definite solubilities in Zn according to the phase diagrams, including Ag (~0.5 at.% at 100 °C), Au (~2 at.% at 0 °C), and Cu (~0.1 at.% at 100 °C). The solubility of Ti in Zn is negligible. Although the solubility of Ag and Cu in Zn at room temperature are not directly available from the phase diagrams, it is reasonable to extrapolate that there will still be some solubility at room temperature. A high potential barrier (~30 mV) is observed on carbon, which is due to the heterogeneous nucleation barrier (Figure 1b, bottom inset). Ti with slight solubility in Zn shows a relatively low potential barrier of 12 mV. Metals including Ag, Cu, and Au exhibit low potential barriers (4 mV for Ag, 7 mV for Cu, and 8 mV for Au) for Zn deposition, which can be attributed to their higher solubilities in Zn. Take Ag as an example, the dissolution of surface Ag into Zn forms a solid-solution surface layer (Figure 1b, top inset), which has an identical crystal structure to that of pure Zn metal (hcp) and thus can serve as a buffer layer and

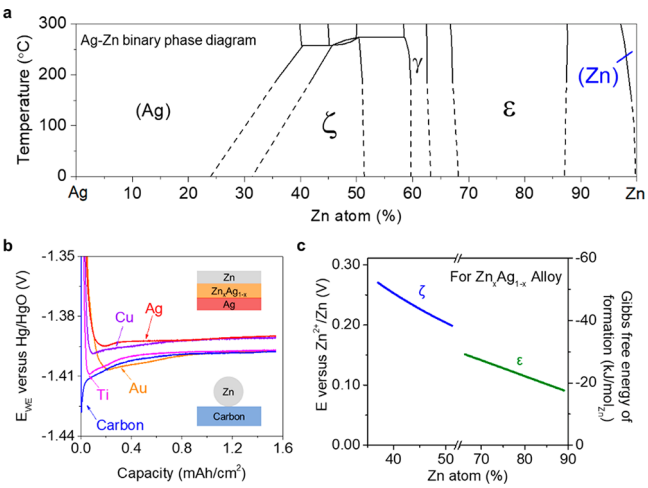

Figure 1. Ag as the seed for electrochemical Zn plating. (a) Phase diagram of Zn with Ag. The region where Ag dissolved in Zn is labeled as (Zn) with a blue color. (b) Voltage profiles of galvanostatic Zn deposition on various substrates at 3 mA cm^{-2}. E_{WE} refers to the potential of the working electrode. Ag showed the lowest potential barrier (~4 mV), and carbon showed the highest potential barrier (~30 mV) for Zn deposition. The insets show the schematic mechanisms of Zn nucleation on Ag and C, which explain the extra energy involved in Zn nucleation on C. Due to the solid solution buffer layer of Ag dissolved in Zn, the nucleation energy was reduced. (c) Calculated Gibbs free energy of formation at room temperature of Zn, ζ- and ε-Zn_xAg_{1-x} alloy phases and the corresponding electrochemical potential shift of Zn^{2+}/Zn_xAg_{1-x} compared with that of Zn^{2+}/Zn.

eliminate nucleation barriers for subsequent Zn deposition. Pt, Ni and Fe have drastically different voltage profiles from above metals, due to their high activities toward hydrogen evolution reaction in alkaline electrolytes.[44] Even though Pt, Ni and Fe can form alloy phases with Zn or are soluble in Zn according to the phase diagrams, no Zn is plated on them as evidenced by their lack of Zn stripping capacity (Figure S2).

We hypothesize that Zn-soluble materials with low nucleation barriers can regulate the deposition of Zn metal. Among the materials we have tested, Ag exhibits the lowest potential barrier of Zn nucleation. Thus, it was chosen to demonstrate the concept. In addition, Ag can react with Zn to form crystalline ζ-, γ-, and ε-Zn_xAg_{1-x} alloy phases, as indicated by the Ag-Zn phase diagram. A computerized calculation of phase diagrams (CALPHAD) technique[45] was used to obtain the Gibbs free energy of formations (Figure 1c) at room temperature of Zn, ζ- and ε-Zn_xAg_{1-x} alloy phases observed in our experiments. The corresponding electrochemical potential shift of Zn^{2+}/Zn_xAg_{1-x} compared with that of Zn^{2+}/Zn was also computed. All of the Zn_xAg_{1-x} alloy phases possess a negative Gibbs free energy of formation, which means that the formation of Zn_xAg_{1-x} is spontaneous during Zn plating. As a result, Ag can potentially be used as a seed to (1) nucleate Zn with a low potential barrier and (2) accommodate Zn by forming alloy phases.

Seeded and Uniform Zn Deposition. To evaluate the possibility of Ag as a seed to spatially control the Zn electrodeposition (Figure 2a), we patterned Ag islands as the seeding material on the C substrate (Figure S3), onto which Zn (0.698 mAh $cm_{electrode}^{-2}$, 2.792 mAh $cm_{Ag\text{-}island}^{-2}$) was galvanostatically deposited at 2.4 mA $cm_{electrode}^{-2}$ (9.6 mA $cm_{Ag\text{-}island}^{-2}$). As shown in the operando optical microscopy

https://doi.org/10.1021/acsenergylett.0c02343
ACS Energy Lett. 2021, 6, 404−412

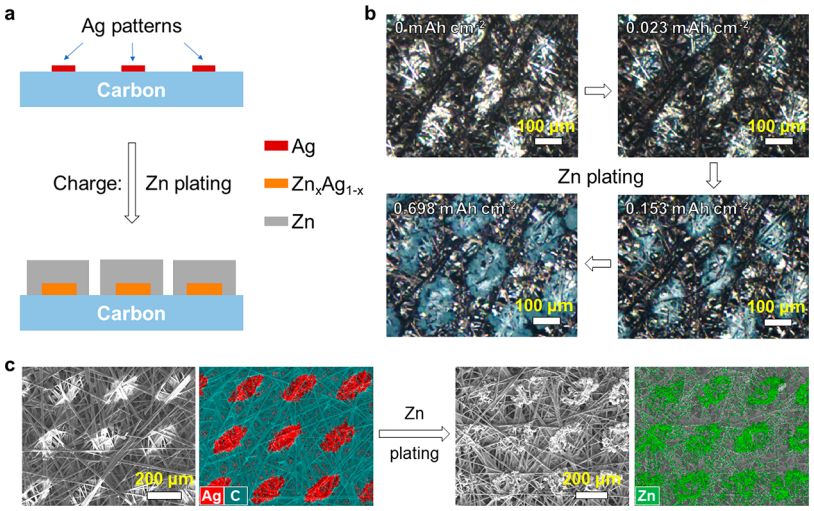

Figure 2. Spatial control of Zn deposition using Ag nuclei. (a) Schematic of the seeded Zn plating on the Ag islands patterned on carbon paper. (b) Operando optical microscopy of the Zn plating (2.4 mA cm^{-2}) on the Ag islands patterned on carbon paper. (c) Scanning electron microscopy (SEM) images and elemental mapping images of the carbon paper coated with patterned Ag islands before and after Zn plating. A seeded deposition of Zn was achieved due to the preferential Zn deposition on Ag.

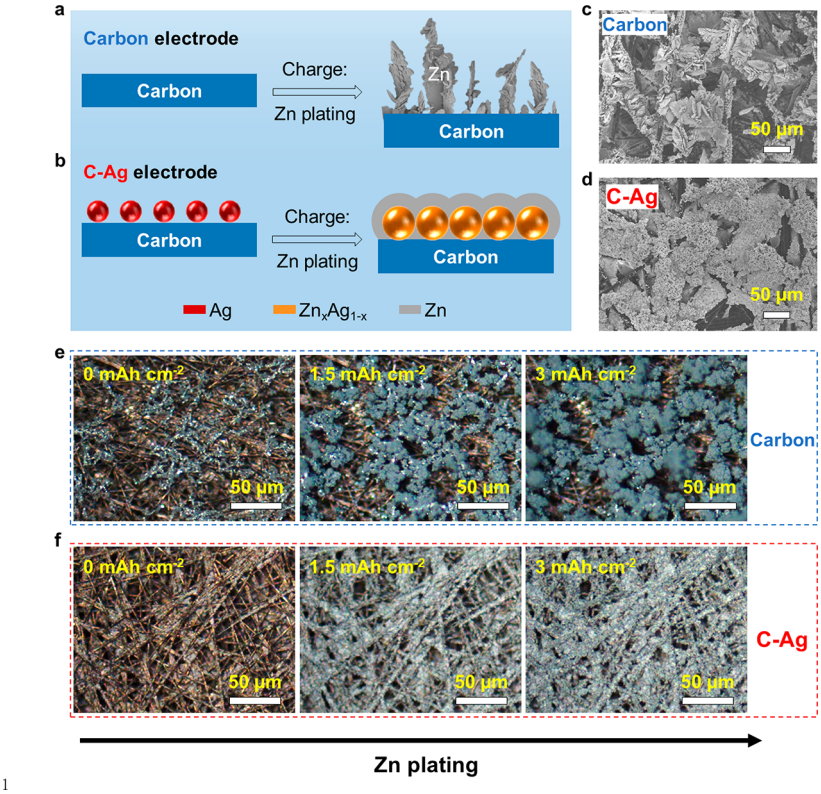

Figure 3. Morphology control of Zn deposition using Ag nuclei. (a) Schematic of nonuniform and dendritic Zn deposition on the carbon paper substrate, which has no solubility in Zn. (b) Schematic of uniform Zn deposition on the carbon paper slurry-coated with Ag nanoparticles. Ag nanoparticles serve as the nucleation sites for the Zn_xAg_{1-x} alloy formation and Zn deposition. (c, d) SEM images of the carbon (c) and C-Ag (d) electrodes after 5.3 mAh cm^{-2} Zn plating (64 mA cm^{-2}). Zn dendrites was only observed on the carbon electrode. (e, f) Operando optical microscopy analysis of Zn plating (18 mA cm^{-2}) on the carbon (e) and C−Ag (f) electrodes. Zn plating on the carbon electrode is mossy, while it is uniform on the C-Ag electrode.

images (Figure 2b, captured from Video 1), most of the Zn was preferentially deposited onto the Ag patterns. A set of operando images with high magnification is shown in Figure S4 (captured from Video 2). EDS mapping (Figure 2c) of the electrode after the Zn deposition process further confirmed the seeded Zn deposition.

Nonuniform and dendritic metal deposition is a well-known problem for Zn anodes (Figure 3a). By spatially controlling and accommodating Zn deposition, a uniform Zn plating is expected to be achieved (Figure 3b). To demonstrate this, we first loaded Ag nanoparticles onto the inert carbon-fiber paper substrate (C-Ag, Figures S5 and S6). Ag nanoparticles and

https://doi.org/10.1021/acsenergylett.0c02343
ACS Energy Lett. 2021, 6, 404−412

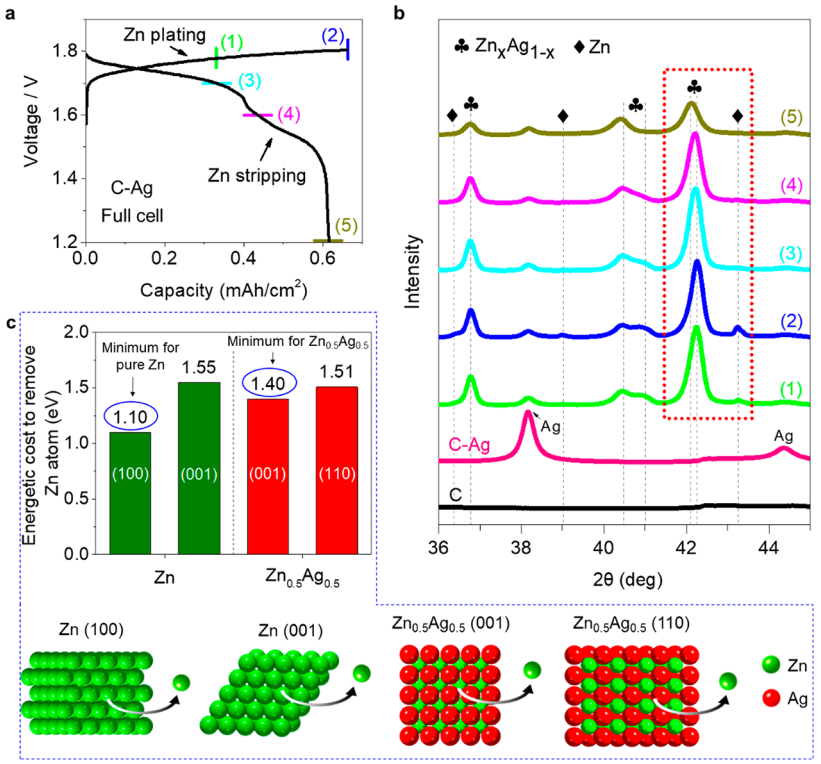

Figure 4. Shift of the stripping potential due to the presence of alloy. (a) Voltage profiles of a full cell containing a C-Ag anode, $Ni(OH)_2$ cathode, and ZnO-saturated 4 M KOH electrolyte. (b) XRD results of the C-Ag electrode at different charge/discharge states, as labeled in (a). The first (1.8−1.6 V) and the second (1.6−1.4 V) discharge plateaus correspond to Zn stripping from the pure Zn metal and the Zn_xAg_{1-x} alloys, respectively (see the red-dashed frame for the reader's convenience). c, DFT simulation results showing the energetic cost of removing a Zn atom from the pure Zn metal and $Zn_{0.5}Ag_{0.5}$ alloy. Constructed models: Zn with 001 and 100 surfaces; $Zn_{0.5}Ag_{0.5}$ with 110 and 001 surfaces.

polyvinylidene difluoride (PVDF) binder were mixed in *N*-methylpyrrolidone, and the resultant slurry was drop-cast onto carbon paper substrates. The diameter of the Ag nanoparticles, which exhibited a face-centered cubic (FCC) structure, was less than 50 nm (Figure S7). We then galvanostatically cycled the carbon paper and C-Ag electrodes in ZnO-saturated 4 M KOH electrolyte and imaged both electrodes ex-situ after Zn plating (5.3 mAh cm^{-2}) at 64 mA cm^{-2}, which was more than twice the mass-transport limiting current density[46,47] (30 mA cm^{-2}, Figure S8). Under such conditions that Zn dendrite formation was favored, dendritic Zn deposition was observed on the carbon paper electrode undoubtedly (Figure 3c). In contrast, nondendritic Zn plating was achieved on the C-Ag electrode (Figures 3d and S9) even at a current density higher than the limited value. Besides, Zn was also plated on the electrodes at a current density of 18 mA cm^{-2}, lower than the mass-transport limit. These electrodes were monitored in operando using an optical microscope. As shown in Figure 3e and Video 3, dendritic Zn was not formed with the operating current below the mass-transport limit, however, mossy and poorly nucleated Zn deposits were observed on the bare carbon paper with high Zn nucleation barrier during charging at the second cycle. In addition, dead Zn that remained from the first cycle was observed on the carbon paper at the beginning of the second charge, and grew in charging, which meant that the dead Zn reconnected to the carbon paper and served as the core for further Zn deposition. The break and reconnection of dead Zn could lead to the instability of Zn anodes (fluctuation of capacity) during battery cycling, as presented in Figure 5a, below. In contrast, the Zn deposited onto the C-Ag electrode with negligible Zn nucleation barrier was uniform, and no dead Zn was observed in the fully discharged state (Figure 3f, captured from Video 4).

Mechanism of Zn Plating/Stripping in the Presence of Alloying Seeds. The C-Ag electrode was assembled into a full Ni-Zn battery using $Ni(OH)_2$ as the cathode and ZnO-saturated 4 M KOH as the electrolyte. The $Zn(OH)_4^{2-}$ from the electrolyte can be electrochemically reduced and deposited onto the C-Ag electrode. The charge capacities were controlled to be 497, 994 and 1491 mAh g_{Ag}^{-1}, so that the molar ratios of deposited Zn to Ag (Zn:Ag) are 1, 2, and 3 assuming no side reactions. In the rest of this article, we use "Zn:Ag = 1", "Zn:Ag = 2" and "Zn:Ag = 3" to represent our charging conditions. The actual Zn:Ag are approximately 0.7, 1.7, and 2.8, respectively, when Coulombic inefficiency is considered. To characterize crystalline Zn_xAg_{1-x} alloys under different charging conditions, we performed ex-situ X-ray diffraction (XRD) for the C-Ag electrode and observed that Zn_xAg_{1-x} alloy phases (ε-, ζ-) were formed successfully (see Figure S10, Table S2 for detailed description of alloy phases and compositions). The formation of Zn_xAg_{1-x} alloys was also confirmed by energy-dispersive X-ray spectroscopy (EDS) mappings (Figure S11).

Upon galvanostatic cycling, the voltage profile (Figure 4a) showed one charge plateau and two apparent discharge plateaus (1.8−1.6 V and 1.6−1.4 V). To probe the phase transitions of the C-Ag electrode during cycling at Zn:Ag = 3, we conducted ex-situ XRD analysis (Figure 4b) of the C-Ag anode at 5 different charge/discharge states, as noted in Figure 4a. The C-Ag electrodes (~0.67 mAh cm^{-2} at Zn:Ag = 3) were charged/discharged at 0.67 mA cm^{-2}. In charged states (1)

https://doi.org/10.1021/acsenergylett.0c02343
ACS Energy Lett. 2021, 6, 404−412

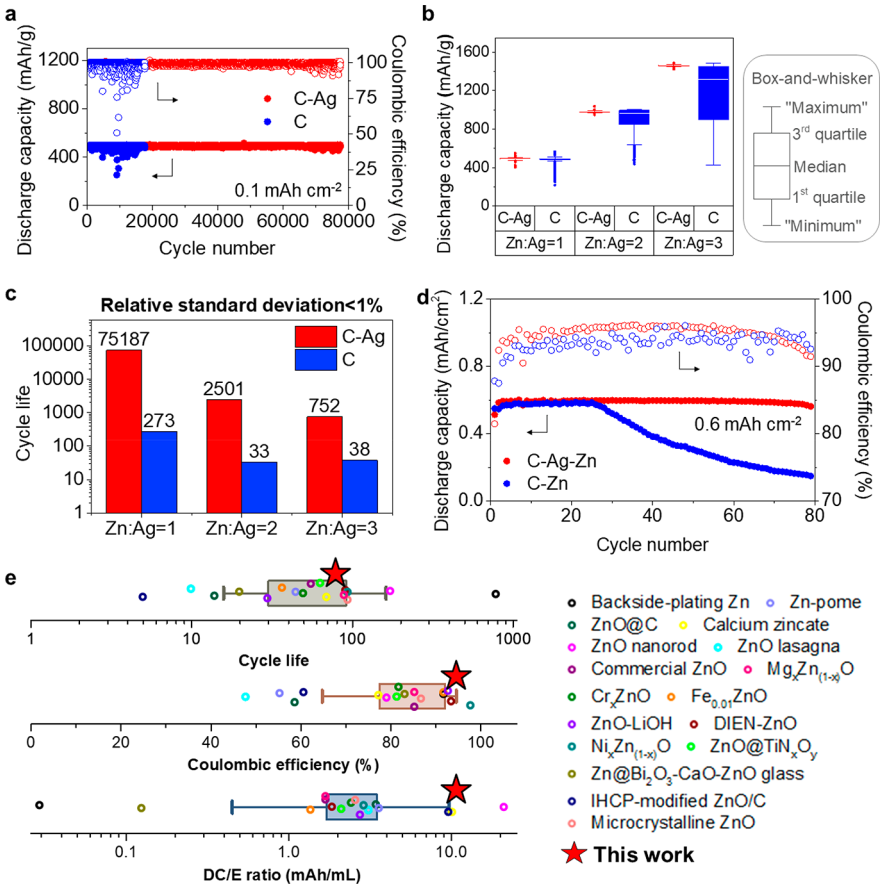

Figure 5. Electrochemical performance of anodes. (a) Cycling performance of the C-Ag and C electrodes at Zn:Ag = 1. (b) Box-and-whisker plot showing distributions of discharge capacities of the C-Ag and C electrodes at Zn:Ag molar ratios ranging from 1 to 3. For Zn:Ag = 1, discharge capacities from the 1st cycle to the 14 980th cycle were used in the box-and-whisker plot. Similarly, the 1st cycle to the 1480th cycle for Zn:Ag = 2 and the 1st cycle to the 630th cycle for Zn:Ag = 3 were used. A summary of five numbers is displayed, including the "minimum" (Q1−1.5*IQR), first quartile (Q1), median, third quartile (Q3), and "maximum" (Q3 + 1.5*IQR). Interquartile range (IQR): 1st to the 3rd quartile. Outliers (values that are located outside the whiskers of the box plot) are marked as red circles. (c) Cycle life comparison of the C-Ag and C electrodes with relative standard deviations of the discharge capacities over cycling being less than 1%. (d) Cycling performance of the C-Ag-Zn and C-Zn anodes charged/discharged at ~2.4 mA cm^{-2}. (e) Box-and-whisker plot showing a comparison between the C-Ag-Zn anode and previously published works in terms of cycle life, Coulombic efficiency, and DC/E ratio.

and (2), the Zn and Zn_xAg_{1-x} alloy phases coexist. During charging from (1) to (2), the peak intensities of Zn increased while the Zn_xAg_{1-x} alloy peaks remained almost unchanged. This result indicates that alloy phases formed prior to the formation of the Zn phase, which is reasonable because alloy phases possess a negative Gibbs free energy of formation. It is counterintuitive that only one charge plateau exists while both Zn and Zn_xAg_{1-x} form. We speculate that the alloy formation rate may be kinetically slower than the Zn deposition rate, which results in only one charge plateau attributed to the Zn^{2+}/Zn redox. Afterward, the Zn and Ag atoms may diffuse slowly to spontaneously form the Zn_xAg_{1-x} alloy. When discharged to state (3), the end of the first discharge plateau, the Zn peak intensity in the corresponding XRD pattern dramatically decreased, while the Zn_xAg_{1-x} alloy peak intensities remained almost unchanged. This result implies that the first discharge plateau (1.8−1.6 V) is mainly attributable to Zn stripping from Zn metal. Upon further discharging, the Zn_xAg_{1-x} alloy peaks decreased at state (4) and their intensities clearly decreased when the battery reached the fully discharged state (5). We concluded that the second discharge plateau (1.6−1.4 V) was associated mainly with Zn stripping from the Zn_xAg_{1-x} alloys, which is consistent with our CALPHAD results that the Zn^{2+}/Zn_xAg_{1-x} redox had a higher potential than Zn^{2+}/Zn. In addition, alloy phases became Zn-leaner during discharging, as evidenced by the negative shift in the characteristic peak positions of the ε-Zn_xAg_{1-x} phase (Figure S9), which also matched our CALPHAD results indicating that Zn-lean alloy phases possessed larger electrochemical potential. We also observed that the Ag nanoparticles could not recover to their original crystal structure after cycling, as evidenced by the unrecovered Ag peaks and the existence of Zn-lean Zn_xAg_{1-x} alloy phases in the fully discharged state (5). The remaining Ag peaks in both the charged and discharged states belong to unreacted Ag nanoparticles, which might be encapsulated by PVDF and thus inactive.

To further understand the Zn stripping process at the atomic level, we simulated models of pure Zn metal and $Zn_{0.5}Ag_{0.5}$ alloy crystals *in silico* and investigated the relative energetic cost of Zn removal from various termination environments using density functional theory (DFT).[48−52] The $Zn_{0.5}Ag_{0.5}$ alloy phase was chosen for the DFT study because it was the phase detected during our experiments; furthermore, its crystal structure is relatively simple. Nanoparticles under cyclic dissolution and reformation in a battery environment display

https://doi.org/10.1021/acsenergylett.0c02343
ACS Energy Lett. 2021, 6, 404−412

a range of morphologies and surface environments. Therefore, two surfaces for each material (Zn metal and $Zn_{0.5}Ag_{0.5}$ alloy) were selected to represent a low-coordination-number environment (100 and 001 surfaces for Zn and $Zn_{0.5}Ag_{0.5}$, respectively) and a high-coordination-number environment (001 and 110 surfaces for Zn and $Zn_{0.5}Ag_{0.5}$, respectively) (Figure S12). We considered multiple possibilities for Zn removal for each slab model to probe the various thermodynamic states in cases of chemically unique Zn atoms. A full report of all of our data is available in Table S3. For the 001 surface termination of $Zn_{0.5}Ag_{0.5}$, both the Zn-terminated and Ag-terminated surfaces were studied, although the Ag-terminated surface was found to be much more energetically stable and thus was the one we considered in our data. We report the minimum energy to remove Zn from each material/termination environment in Figure 4c. The minimum energy to remove Zn was 1.10 eV for Zn with a 100 surface termination and 1.40 eV for $Zn_{0.5}Ag_{0.5}$ with a 001 surface termination, which indicates the Zn atom is less reactive in the $Zn_{0.5}Ag_{0.5}$ alloy than in the pure Zn metal. These DFT results provide some insight into the more energetic Zn stripping process from Zn_xAg_{1-x} alloys and thus higher electrochemical potential of the Zn^{2+}/Zn_xAg_{1-x} redox than the Zn^{2+}/Zn redox, which can also explain the anticorrosion property of Zn alloy phases reported recently.[29,38−40]

To confirm that the two discharge plateaus of the full battery were caused by the C-Ag anode instead of the $Ni(OH)_2$ cathode, the voltage profile of a full Ni-Zn battery using the carbon paper as the anode is presented in Figure S13. Only one discharge plateau was observed when Ag was not added to the anode. We also carried out cyclic voltammetry (CV) of the C-Ag electrode using a three-electrode electrochemical cell that consisted of the substrate of interest as the working electrode, Hg/HgO as the reference electrode, Zn foil as the counter electrode and a ZnO-saturated 4 M KOH aqueous solution as the electrolyte. The result was in good agreement with our analysis that the two discharge plateaus were due to the different electrochemical potentials of the Zn^{2+}/Zn and Zn^{2+}/Zn_xAg_{1-x} redox reactions on the C-Ag electrode (Figure S14).

Stable Cycling of Ag-Seeded Zn Anodes. In previous sections, the spatially controlled and uniform Zn deposition on the Ag seeds was demonstrated and investigated. To further evaluate the cyclic stability of Ag-seeded Zn anodes (C-Ag), pouch-type Ni-Zn batteries were assembled and tested. Batteries with bare C anodes were also assembled and tested under the same conditions. During charging, zincates dissolved in the electrolyte were electrochemically reduced at the anode. Less than 7.5% of zincates from the electrolyte were consumed in each cycle, to minimize the hydrogen evolution side reaction.

As shown in the cycling results (Figures 5a and S15−S17), instead of steady capacity decay, batteries undergo irregular capacity decay with intensified fluctuations of capacity over cycling, which is indicative of battery degradation. To better analyze the cyclic stabilities of the C-Ag and C electrodes, we constructed a box-and-whisker plot to show the statistic distributions of their discharge capacities over cycling (Figure 5b), where a summary of five numbers is displayed, including the "minimum", first quartile, median, third quartile, and "maximum" discharge capacities. Three Zn:Ag ratios (1, 2, and 3) were tested. Correspondingly, the areal capacities were ∼0.1, ∼0.2, and ∼0.3 mAh cm^{-2} with charge/discharge current density of ∼2.4 mA cm^{-2}. At all Zn:Ag ratios, the C-Ag electrodes demonstrated higher cyclic stability with less fluctuation of capacity than the C electrodes. In addition, the C-Ag electrodes also achieved a higher average discharge capacity and Coulombic efficiency than the C electrodes: 491.7 mAh g^{-1} and 99.0% for C-Ag vs 487.3 mAh g^{-1} and 98.1% for C at Zn:Ag = 1; 983.7 mAh g^{-1} and 99.1% for C-Ag vs 893.1 mAh g^{-1} and 97.3% for C at Zn:Ag = 2; 1458.9 mAh g^{-1} and 98.0% for C-Ag vs 1175.4 mAh g^{-1} and 96.7% for C at Zn:Ag = 3. The above statistical analysis was done within limited cycle ranges for C-Ag and C electrodes: 14980 cycles for Zn:Ag = 1, 1480 cycles for Zn:Ag = 2, and 630 cycles for Zn:Ag = 3. Due to the irregular capacity decay, the cycle life was defined as the cycle number when the relative standard deviation of discharge capacities exceeds 1%. As shown in Figure 5c, the C-Ag electrodes exhibited superior cycle lives of 75187, 2501, and 752 cycles when cycled at Zn:Ag ratios ranging from 1 to 3, respectively, while the C electrodes exhibited 273, 33, and 38 cycles, respectively. The dendritic Zn plating and break/reconnection of partial dead Zn could have led to the capacity fluctuation of C electrodes, which was visualized under the optical microscope (Figure 3e). In addition, the resultant unstable electrode−electrolyte interface and severe electrolyte decomposition (reacting with dead Zn and evolving H_2) might explain the capacity decay of C electrodes. With a simple Ag nanoparticle loading process, a spatially controlled and uniform Zn deposition through heterogeneous seeded growth is achieved, leading to the superior long-term cyclic stability of the C-Ag electrodes.

The discharge capacity/electrolyte (DC/E) ratio is an important indicator for device-level energy density.[53−55] The DC/E ratio of the cells shown in Figure 5a−c was lower than 0.8 mAh mL^{-1} because they utilized a small percentage of the zincates available from the electrolyte. To demonstrate the effect of Ag seeds on Zn anodes at a higher DC/E ratio, we predeposited ∼1 mAh cm^{-2} Zn onto the C and C-Ag electrodes and assembled Ni-Zn full cells. As shown in Figure 5d, the C-Ag-Zn anode achieved superior cycling performance, with a Coulombic efficiency of 95% for 78 cycles; the C-Zn anode performed with a Coulombic efficiency of 92.6% for 25 cycles, which implied that the Ag addition also improved the Zn anode even at a high DC/E ratio (12 mAh mL^{-1}). The simple loading of Ag nanoparticles onto the Zn anode, without any complex structural or molecular design, improved its cycling performance to be comprehensively superior to that of previously reported, deeply cycled Zn anodes[56−71] (Table S4) with 100% depth-of-discharge in alkaline electrolytes (Figure 5e). Three parameters (cycle life, Coulombic efficiency, and DC/E ratio) were considered in the comparison. Notably, it was less meaningful to compare only one or two parameters; thus, only publications that reported all three values or provided necessary information to calculate them were included in our comparison. Partially discharged metallic zinc anodes were not included for comparison either, because their discharge capacity (and therefore Coulombic efficiency) is artificially controlled and cannot reflect the intrinsic property of the anodes.

When considering the mass of the carbon paper substrate, the overall areal and specific discharge capacities of the C-Ag-Zn anode were ∼0.6 mAh cm^{-2} and ∼52 mAh g^{-1}, respectively, which are not ready for practical applications.[55] However, the mechanistic understanding and design principles of spatial control of Zn deposition reported here may be adopted in state-of-the-art Zn anodes, particularly those with

https://doi.org/10.1021/acsenergylett.0c02343
ACS Energy Lett. 2021, 6, 404−412

high areal loadings, to approach a practically relevant Zn anode for rechargeable aqueous batteries.

Besides carbon paper substrate, seeded Zn deposition was also achieved on Ag-patterned stainless steel and Ni substrates (Figures S18 and S19, Videos 5 and 6). Yet the self-discharge of Zn and the hydrogen evolution on these patterned substrates were severe due to the high hydrogen evolution activities of stainless steel and Ni in alkaline electrolytes (Videos 7 and 8). Regarding the choice of seeding materials that can alloy with Zn, we have evaluated the commercial viability of using Ag seeds from aspects of cost and energy density (Figures S20–S23). Ag alloy anode has the potential to be commercialized, especially when high-energy-density batteries or batteries with long cycle life are needed. Cu lowers the potential barrier for Zn deposition as well (Figure 1b), and has lower cost than Ag. Thus, Cu is a promising choice of Zn-alloying seed for large-scale applications.

Even though this study was conducted using alkaline electrolytes, our mechanistic understandings might also be applicable to Zn anodes operating in neutral and acidic electrolytes. Seeded growth of Zn on the Ag islands patterned on carbon paper was also achieved in a mildly acidic 2 M $ZnSO_4$ electrolyte (Figure S24). In addition, we have investigated Zn metal deposition onto various substrates in the 2 M $ZnSO_4$ electrolyte, including Ag, Cu, Fe, Ni, Au, Pt, Ti, and C. Specifically, 100 nm of the corresponding metal film was evaporated onto a Cu foil. Then, three-electrode electrochemical cells were constructed that consisted of the substrate of interest as the working electrode, Zn foil as the reference electrode and Zn foil as the counter electrode. Zn metal was galvanostatically plated and stripped in the 2 M $ZnSO_4$ electrolyte. As shown in the voltage profiles (Figure S25), Cu, Ag, and Fe might be good candidates to modify Zn anodes for use in mildly acidic electrolytes in terms of both Zn nucleation barrier and Coulombic efficiency.

In conclusion, we reported the mechanisms for the regulation of Zn electrodeposition on alloy anodes through comprehensive analysis for the first time. As a proof of concept, Ag loaded on an inert carbon paper substrate achieved a spatially controlled and uniform Zn deposition through heterogeneous seeded growth. Ag has two functions: (1) Ag, with a definite solubility in Zn, could help eliminate the heterogeneous Zn nucleation barrier and (2) the formation of Zn_xAg_{1-x} alloy phases occurs preferentially during Zn plating because of their negative Gibbs free energy of formation. As a result, the Ag nanoparticle-loaded carbon paper (C-Ag) achieved superior long-term cyclic stability compared with the C electrode. The results of density functional theory suggest a more energetic Zn stripping process from Zn_xAg_{1-x} alloys and thus higher electrochemical potential of the Zn^{2+}/Zn_xAg_{1-x} redox than the Zn^{2+}/Zn redox, which can also explain the anti-corrosion property of Zn alloy phases. In addition, the seeded Zn deposition was visualized in operando for the first time using an optical microscope. Our findings can potentially guide the future design of high-performance Zn anodes in alkaline electrolytes. Similar mechanisms are expected for Zn anodes operating in neutral and acidic electrolytes as well as other metal anodes (e.g., Al, Mg, Na, K).

■ ASSOCIATED CONTENT

Supporting Information

The Supporting Information is available free of charge at https://pubs.acs.org/doi/10.1021/acsenergylett.0c02343.

Experimental method, DFT simulation, additional electrochemical and characterization results, and captions for the supplementary videos (PDF)

Supplementary Video 1 (MP4)

Supplementary Video 2 (MP4)

Supplementary Video 3 (MP4)

Supplementary Video 4 (MP4)

Supplementary Video 5 (MP4)

Supplementary Video 6 (MP4)

Supplementary Video 7 (MP4)

Supplementary Video 8 (MP4)

■ AUTHOR INFORMATION

Corresponding Author

Nian Liu − *School of Chemical and Biomolecular Engineering, Georgia Institute of Technology, Atlanta, Georgia 30332, United States;* orcid.org/0000-0002-5966-0244; Email: nian.liu@chbe.gatech.edu

Authors

Yamin Zhang − *School of Chemical and Biomolecular Engineering, Georgia Institute of Technology, Atlanta, Georgia 30332, United States;* orcid.org/0000-0003-4890-1265

Joshua D. Howe − *School of Chemical and Biomolecular Engineering, Georgia Institute of Technology, Atlanta, Georgia 30332, United States; Department of Chemical Engineering, Texas Tech University, Lubbock, Texas 79409, United States;* orcid.org/0000-0002-6628-8532

Sarah Ben-Yoseph − *School of Chemical and Biomolecular Engineering, Georgia Institute of Technology, Atlanta, Georgia 30332, United States*

Yutong Wu − *School of Chemical and Biomolecular Engineering, Georgia Institute of Technology, Atlanta, Georgia 30332, United States;* orcid.org/0000-0003-1214-9147

Complete contact information is available at: https://pubs.acs.org/10.1021/acsenergylett.0c02343

Author Contributions

Y.Z. and N.L. conceived the idea and co-wrote the manuscript. Y.Z. carried out the synthesis, material characterization, and electrochemical measurements. J.H. conducted the simulation. S.B.-Y. and Y.W. assisted with material characterization and electrochemical measurements. All authors discussed the results and commented on the manuscript.

Notes

The authors declare no competing financial interest.

■ ACKNOWLEDGMENTS

N.L. acknowledges support from faculty startup funds from the Georgia Institute of Technology. The authors thank Prof. David S. Sholl and David Tavakoli for useful discussions. Anmol Mathur, Jingxuan Chen, Harsh H. Patel, and Yifan Zhang are acknowledged for their experimental support. Material characterization was performed in part at the Georgia Tech Institute for Electronics and Nanotechnology, a member of the National Nanotechnology Coordinated Infrastructure, which is supported by the National Science Foundation (Grant ECCS-1542174).

REFERENCES

(1) Chu, S.; Cui, Y.; Liu, N. The Path towards Sustainable Energy. *Nat. Mater.* **2017**, *16* (1), 16−22.

(2) Zhang, Y.; Liu, N. Nanostructured Electrode Materials for High-Energy Rechargeable Li, Na and Zn Batteries. *Chem. Mater.* **2017**, *29* (22), 9589−9604.

(3) Kim, H.; Hong, J.; Park, K. Y.; Kim, H.; Kim, S. W.; Kang, K. Aqueous Rechargeable Li and Na Ion Batteries. *Chem. Rev.* **2014**, *114* (23), 11788−11827.

(4) Lin, K.; Chen, Q.; Gerhardt, M. R.; Tong, L.; Kim, S. B.; Eisenach, L.; Valle, A. W.; Hardee, D.; Gordon, R. G.; Aziz, M. J.; et al. Alkaline Quinone Flow Battery. *Science* **2015**, *349* (6255), 1529−1532.

(5) Liang, Y.; Jing, Y.; Gheytani, S.; Lee, K. Y.; Liu, P.; Facchetti, A.; Yao, Y. Universal Quinone Electrodes for Long Cycle Life Aqueous Rechargeable Batteries. *Nat. Mater.* **2017**, *16* (8), 841−848.

(6) Luo, J.-Y.; Cui, W.-J.; He, P.; Xia, Y.-Y. Raising the Cycling Stability of Aqueous Lithium-Ion Batteries by Eliminating Oxygen in the Electrolyte. *Nat. Chem.* **2010**, *2* (9), 760−765.

(7) Xie, J.; Zhang, Q. Recent Progress in Multivalent Metal (Mg, Zn, Ca, and Al) and Metal-Ion Rechargeable Batteries with Organic Materials as Promising Electrodes. *Small* **2019**, *15*, 1805061.

(8) Chen, W.; Li, G.; Pei, A.; Li, Y.; Liao, L.; Wang, H.; Wan, J.; Liang, Z.; Chen, G.; Zhang, H.; et al. A Manganese−Hydrogen Battery with Potential for Grid-Scale Energy Storage. *Nat. Energy* **2018**, *3* (5), 428−435.

(9) Wang, F.; Borodin, O.; Gao, T.; Fan, X.; Sun, W.; Han, F.; Faraone, A.; Dura, J. A.; Xu, K.; Wang, C. Highly Reversible Zinc Metal Anode for Aqueous Batteries. *Nat. Mater.* **2018**, *17* (6), 543−549.

(10) Pan, H.; Shao, Y.; Yan, P.; Cheng, Y.; Han, K. S.; Nie, Z.; Wang, C.; Yang, J.; Li, X.; Bhattacharya, P.; et al. Reversible Aqueous Zinc/Manganese Oxide Energy Storage from Conversion Reactions. *Nat. Energy* **2016**, *1* (5), 16039.

(11) Zhang, N.; Cheng, F.; Liu, J.; Wang, L.; Long, X.; Liu, X.; Li, F.; Chen, J. Rechargeable Aqueous Zinc-Manganese Dioxide Batteries with High Energy and Power Densities. *Nat. Commun.* **2017**, *8* (1), 405.

(12) Wu, T.-H.; Zhang, Y.; Althouse, Z. D.; Liu, N. Nanoscale Design of Zinc Anodes for High-Energy Aqueous Rechargeable Batteries. *Mater. Today Nano* **2019**, *6*, 100032.

(13) Zhong, C.; Liu, B.; Ding, J.; Liu, X.; Zhong, Y.; Li, Y.; Sun, C.; Han, X.; Deng, Y.; Zhao, N.; et al. Decoupling Electrolytes towards Stable and High-Energy Rechargeable Aqueous Zinc−Manganese Dioxide Batteries. *Nat. Energy* **2020**, *5* (6), 440−449.

(14) Ma, J.; Sung, J.; Hong, J.; Chae, S.; Kim, N.; Choi, S.-H.; Nam, G.; Son, Y.; Kim, S. Y.; Ko, M.; et al. Towards Maximized Volumetric Capacity via Pore-Coordinated Design for Large-Volume-Change Lithium-Ion Battery Anodes. *Nat. Commun.* **2019**, *10* (1), 475.

(15) Liu, K.; Liu, W.; Qiu, Y.; Kong, B.; Sun, Y.; Chen, Z.; Zhuo, D.; Lin, D.; Cui, Y. Electrospun Core-Shell Microfiber Separator with Thermal-Triggered Flame-Retardant Properties for Lithium-Ion Batteries. *Sci. Adv.* **2017**, *3* (1), No. e1601978.

(16) Li, Y.; Li, Y.; Pei, A.; Yan, K.; Sun, Y.; Wu, C.-L.; Joubert, L.-M.; Chin, R.; Koh, A. L.; Yu, Y.; et al. Atomic Structure of Sensitive Battery Materials and Interfaces Revealed by Cryo−Electron Microscopy. *Science* **2017**, *358* (6362), 506−510.

(17) Zheng, J.; Zhao, Q.; Tang, T.; Yin, J.; Quilty, C. D.; Renderos, G. D.; Liu, X.; Deng, Y.; Wang, L.; Bock, D. C.; et al. Reversible Epitaxial Electrodeposition of Metals in Battery Anodes. *Science* **2019**, *366* (6465), 645−648.

(18) Zhou, Z.; Zhang, Y.; Chen, P.; Wu, Y.; Yang, H.; Ding, H.; Zhang, Y.; Wang, Z.; Du, X.; Liu, N. Graphene Oxide-Modified Zinc Anode for Rechargeable Aqueous Batteries. *Chem. Eng. Sci.* **2019**, *194*, 142−147.

(19) Parker, J. F.; Chervin, C. N.; Pala, I. R.; Machler, M.; Burz, M. F.; Long, J. W.; Rolison, D. R. Rechargeable Nickel-3D Zinc Batteries: An Energy-Dense, Safer Alternative to Lithium-Ion. *Science* **2017**, *356* (6336), 415−418.

(20) Nam, K. W.; Kim, H.; Beldjoudi, Y.; Kwon, T.; Kim, D. J.; Stoddart, J. F. Redox-Active Phenanthrenequinone Triangles in Aqueous Rechargeable Zinc Batteries. *J. Am. Chem. Soc.* **2020**, *142* (5), 2541−2548.

(21) Li, Y.; Dai, H. Recent Advances in Zinc-Air Batteries. *Chem. Soc. Rev.* **2014**, *43* (15), 5257−5275.

(22) Fu, J.; Liang, R.; Liu, G.; Yu, A.; Bai, Z.; Yang, L.; Chen, Z. Recent Progress in Electrically Rechargeable Zinc−Air Batteries. *Adv. Mater.* **2019**, *31* (31), 1805230.

(23) Li, Y.; Lu, J. Metal−Air Batteries: Will They Be the Future Electrochemical Energy Storage Device of Choice? *ACS Energy Lett.* **2017**, *2* (6), 1370−1377.

(24) Zhang, J.; Zhou, Q.; Tang, Y.; Zhang, L.; Li, Y. Zinc−Air Batteries: Are They Ready for Prime Time? *Chem. Sci.* **2019**, *10* (39), 8924−8929.

(25) Tang, T.; Jiang, W.-J.; Liu, X.-Z.; Deng, J.; Niu, S.; Wang, B.; Jin, S.-F.; Zhang, Q.; Gu, L.; Hu, J.-S.; et al. Metastable Rock Salt Oxide-Mediated Synthesis of High-Density Dual-Protected M@NC for Long-Life Rechargeable Zinc−Air Batteries with Record Power Density. *J. Am. Chem. Soc.* **2020**, *142* (15), 7116−7127.

(26) Yufit, V.; Tariq, F.; Eastwood, D. S.; Biton, M.; Wu, B.; Lee, P. D.; Brandon, N. P. Operando Visualization and Multi-Scale Tomography Studies of Dendrite Formation and Dissolution in Zinc Batteries. *Joule* **2019**, *3* (2), 485−502.

(27) Zhang, Q.; Luan, J.; Tang, Y.; Ji, X.; Wang, H. Interfacial Design of Dendrite-Free Zinc Anodes for Aqueous Zinc-Ion Batteries. *Angew. Chem., Int. Ed.* **2020**, *59* (32), 13180−13191.

(28) Cui, M.; Xiao, Y.; Kang, L.; Du, W.; Gao, Y.; Sun, X.; Zhou, Y.; Li, X.; Li, H.; Jiang, F.; et al. Quasi-Isolated Au Particles as Heterogeneous Seeds To Guide Uniform Zn Deposition for Aqueous Zinc-Ion Batteries. *ACS Appl. Energy Mater.* **2019**, *2* (9), 6490−6496.

(29) Yu, J.; Chen, F.; Tang, Q.; Gebremariam, T. T.; Wang, J.; Gong, X.; Wang, X. Ag-Modified Cu Foams as Three-Dimensional Anodes for Rechargeable Zinc−Air Batteries. *ACS Appl. Nano Mater.* **2019**, *2* (5), 2679−2688.

(30) Guo, W.; Yang, C.; Zhao, Z.; Xin, X.; Tian, Z.; Peng, K.; Lai, Y. MOFs Derived Ag/ZnO Nanocomposites Anode for Zn/Ni Batteries. *J. Solid State Chem.* **2019**, *272*, 27−31.

(31) Yang, B.; Yang, Z.; Wang, R.; Feng, Z. Silver Nanoparticle Deposited Layered Double Hydroxide Nanosheets as a Novel and High-Performing Anode Material for Enhanced Ni-Zn Secondary Batteries. *J. Mater. Chem. A* **2014**, *2* (3), 785−791.

(32) Yang, B.; Yang, Z.; Wang, R. Facile Synthesis of Novel Two-Dimensional Silver-Coated Layered Double Hydroxide Nanosheets as Advanced Anode Material for Ni-Zn Secondary Batteries. *J. Power Sources* **2014**, *251*, 14−19.

(33) Huang, J.; Yang, Z. A One-Pot Method to Prepare a ZnO/Ag/Polypyrrole Composite for Zinc Alkaline Secondary Batteries. *RSC Adv.* **2015**, *5* (43), 33814−33817.

(34) Wu, J. Z.; Tu, J. P.; Yuan, Y. F.; Ma, M.; Wang, X. L.; Zhang, L.; Li, R. L.; Zhang, J. Ag-Modification Improving the Electrochemical Performance of ZnO Anode for Ni/Zn Secondary Batteries. *J. Alloys Compd.* **2009**, *479* (1−2), 624−628.

(35) Huang, J.; Yang, Z.; Feng, Z.; Xie, X.; Wen, X. A Novel ZnO@Ag@Polypyrrole Hybrid Composite Evaluated as Anode Material for Zinc-Based Secondary Cell. *Sci. Rep.* **2016**, *6* (1), 24471.

(36) Shi, X.; Xu, G.; Liang, S.; Li, C.; Guo, S.; Xie, X.; Ma, X.; Zhou, J. Homogeneous Deposition of Zinc on Three-Dimensional Porous Copper Foam as a Superior Zinc Metal Anode. *ACS Sustainable Chem. Eng.* **2019**, *7* (21), 17737−17746.

(37) Liu, B.; Wang, S.; Wang, Z.; Lei, H.; Chen, Z.; Mai, W. Novel 3D Nanoporous Zn−Cu Alloy as Long-Life Anode toward High-Voltage Double Electrolyte Aqueous Zinc-Ion Batteries. *Small* **2020**, *16* (22), 2001323.

(38) Cai, Z.; Ou, Y.; Wang, J.; Xiao, R.; Fu, L.; Yuan, Z.; Zhan, R.; Sun, Y. Chemically Resistant Cu-Zn/Zn Composite Anode for Long Cycling Aqueous Batteries. *Energy Storage Mater.* **2020**, *27*, 205−211.

(39) Durmus, Y. E.; Montiel Guerrero, S. S.; Tempel, H.; Hausen, F.; Kungl, H.; Eichel, R.-A. Influence of Al Alloying on the

https://doi.org/10.1021/acsenergylett.0c02343
ACS Energy Lett. 2021, 6, 404−412

Electrochemical Behavior of Zn Electrodes for Zn−Air Batteries With Neutral Sodium Chloride Electrolyte. *Front. Chem.* **2019**, *7*, 800.
(40) Elrouby, M.; El −Shafy Shilkamy, H. A.; Elsayed, A. Development of the Electrochemical Performance of Zinc via Alloying with Indium as Anode for Alkaline Batteries Application. *J. Alloys Compd.* **2021**, *854*, 157285.
(41) Massalski, T. B.; Okamoto, H. *Binary Alloy Phase Diagrams*; ASM International: Materials Park, OH, 1990.
(42) Lim, M. B.; Lambert, T. N.; Ruiz, E. I. Effect of ZnO-Saturated Electrolyte on Rechargeable Alkaline Zinc Batteries at Increased Depth-of-Discharge. *J. Electrochem. Soc.* **2020**, *167* (6), 060508.
(43) Yan, K.; Lu, Z.; Lee, H.-W.; Xiong, F.; Hsu, P.-C.; Li, Y.; Zhao, J.; Chu, S.; Cui, Y. Selective Deposition and Stable Encapsulation of Lithium through Heterogeneous Seeded Growth. *Nat. Energy* **2016**, *1* (3), 16010.
(44) Wei, X.; Desai, D.; Yadav, G. G.; Turney, D. E.; Couzis, A.; Banerjee, S. Impact of Anode Substrates on Electrodeposited Zinc over Cycling in Zinc-Anode Rechargeable Alkaline Batteries. *Electrochim. Acta* **2016**, *212*, 603−613.
(45) Gómez-Acebo, T. Thermodynamic Assessment of the Ag-Zn System. *CALPHAD: Comput. Coupling Phase Diagrams Thermochem.* **1998**, *22* (2), 203−220.
(46) Banik, S. J.; Akolkar, R. Suppressing Dendritic Growth during Alkaline Zinc Electrodeposition Using Polyethylenimine Additive. *Electrochim. Acta* **2015**, *179*, 475−481.
(47) Banik, S. J.; Akolkar, R. Suppressing Dendrite Growth during Zinc Electrodeposition by PEG-200 Additive. *J. Electrochem. Soc.* **2013**, *160* (11), D519−D523.
(48) Kresse, G.; Furthmüller, J. Efficiency of Ab-Initio Total Energy Calculations for Metals and Semiconductors Using a Plane-Wave Basis Set. *Comput. Mater. Sci.* **1996**, *6* (1), 15−50.
(49) Kresse, G.; Furthmüller, J. Efficient Iterative Schemes for Ab Initio Total-Energy Calculations Using a Plane-Wave Basis Set. *Phys. Rev. B: Condens. Matter Mater. Phys.* **1996**, *54* (16), 11169−11186.
(50) Perdew, J. P.; Burke, K.; Ernzerhof, M. Generalized Gradient Approximation Made Simple. *Phys. Rev. Lett.* **1996**, *77* (18), 3865−3868.
(51) Blöchl, P. E. Projector Augmented-Wave Method. *Phys. Rev. B: Condens. Matter Mater. Phys.* **1994**, *50* (24), 17953−17979.
(52) Monkhorst, H. J.; Pack, J. D. Special Points for Brillouin-Zone Integrations. *Phys. Rev. B* **1976**, *13* (12), 5188−5192.
(53) Zhang, Y.; Wu, Y.; You, W.; Tian, M.; Huang, P.-W.; Zhang, Y.; Sun, Z.; Ma, Y.; Hao, T.; Liu, N. Deeply Rechargeable and Hydrogen-Evolution-Suppressing Zinc Anode in Alkaline Aqueous Electrolyte. *Nano Lett.* **2020**, *20* (6), 4700−4707.
(54) Turney, D. E.; Gallaway, J. W.; Yadav, G. G.; Ramirez, R.; Nyce, M.; Banerjee, S.; Chen-Wiegart, Y. K.; Wang, J.; D'Ambrose, M. J.; Kolhekar, S.; et al. Rechargeable Zinc Alkaline Anodes for Long-Cycle Energy Storage. *Chem. Mater.* **2017**, *29* (11), 4819−4832.
(55) Parker, J. F.; Ko, J. S.; Rolison, D. R.; Long, J. W. Translating Materials-Level Performance into Device-Relevant Metrics for Zinc-Based Batteries. *Joule* **2018**, *2* (12), 2519−2527.
(56) Higashi, S.; Lee, S. W.; Lee, J. S.; Takechi, K.; Cui, Y. Avoiding Short Circuits from Zinc Metal Dendrites in Anode by Backside-Plating Configuration. *Nat. Commun.* **2016**, *7* (1), 11801.
(57) Wu, Y.; Zhang, Y.; Ma, Y.; Howe, J. D.; Yang, H.; Chen, P.; Aluri, S.; Liu, N. Ion-Sieving Carbon Nanoshells for Deeply Rechargeable Zn-Based Aqueous Batteries. *Adv. Energy Mater.* **2018**, *8* (36), 1802470.
(58) Kang, S.; Im, Y.; Park, K. S.; Cho, T. W.; Jeon, J.; Chung, K.; Kang, M. The Incorporation of Cr Ions into the Framework of ZnO for Stable Electrochemical Performance in a Membrane Free Alkaline Ni/Zn Redox. *Electrochim. Acta* **2016**, *209*, 623−631.
(59) Im, Y.; Kim, K. M.; Park, K. S.; Cho, T. W.; Jeon, J.; Chung, K.; Kang, M. Inhibition of Zn Dendrite Growth Using Ni x Zn (1-x) O Anodic Material during a Redox Cycling Test in Zn/Ni Battery. *Solid State Ionics* **2016**, *295*, 13−24.
(60) Kwak, B. S.; Jo, S. W.; Park, K. S.; Cho, T. W.; Jeon, J.; Chung, K.; Kang, M. Synthesis of Microcrystalline ZnO as an Anodic Material via a Solvothermal Method, and Its Electrochemical Performance in Ni/Zn Redox Battery. *J. Ind. Eng. Chem.* **2017**, *46*, 111−118.
(61) Kwak, B. S.; Kim, D. Y.; Park, S. S.; Kim, B. S.; Kang, M. Implementation of Stable Electrochemical Performance Using a Fe0.01ZnO Anodic Material in Alkaline Ni-Zn Redox Battery. *Chem. Eng. J.* **2015**, *281*, 368−378.
(62) Im, Y.; Kang, S.; Kwak, B. S.; Park, K. S.; Cho, T. W.; Lee, J.-S.; Kang, M. Electrochemical Performance of Three Shaped ZnO Nanoparticles Prepared in LiOH, NaOH and KOH Alkaline Solutions as Anodic Materials for Ni/Zn Redox Batteries. *Korean J. Chem. Eng.* **2016**, *33* (4), 1447−1455.
(63) Im, Y.; Kim, J.; Park, K. S.; Cho, T. W.; Jeon, J.; Chung, K.; Eguchi, K.; Kang, M. Influence of Small Amount of Mg Incorporated into Hexagonal ZnO Crystal on Cell Performance in Membrane Free Zinc−Nickel Redox Battery. *J. Ind. Eng. Chem.* **2018**, *64*, 318−327.
(64) Zhang, Y.; Wu, Y.; Ding, H.; Yan, Y.; Zhou, Z.; Ding, Y.; Liu, N. Sealing ZnO Nanorods for Deeply Rechargeable High-Energy Aqueous Battery Anodes. *Nano Energy* **2018**, *53*, 666−674.
(65) Chen, P.; Wu, Y.; Zhang, Y.; Wu, T.-H.; Ma, Y.; Pelkowski, C.; Yang, H.; Zhang, Y.; Hu, X.; Liu, N. A Deeply Rechargeable Zinc Anode with Pomegranate-Inspired Nanostructure for High-Energy Aqueous Batteries. *J. Mater. Chem. A* **2018**, *6* (44), 21933−21940.
(66) Yan, Y.; Zhang, Y.; Wu, Y.; Wang, Z.; Mathur, A.; Yang, H.; Chen, P.; Nair, S.; Liu, N. A Lasagna-Inspired Nanoscale ZnO Anode Design for High-Energy Rechargeable Aqueous Batteries. *ACS Appl. Energy Mater.* **2018**, *1* (11), 6345−6351.
(67) Yuan, Y. F.; Tu, J. P.; Wu, H. M.; Li, Y.; Shi, D. Q. Size and Morphology Effects of ZnO Anode Nanomaterials for Zn/Ni Secondary Batteries. *Nanotechnology* **2005**, *16* (6), 803−808.
(68) Zhang, C.; Wang, J. M.; Zhang, L.; Zhang, J. Q.; Cao, C. N. Study of the Performance of Secondary Alkaline Pasted Zinc Electrodes. *J. Appl. Electrochem.* **2001**, *31* (9), 1049−1054.
(69) Michlik, T.; Schmid, M.; Rosin, A.; Gerdes, T.; Moos, R. Mechanical Coating of Zinc Particles with Bi2O3-Li2O-ZnO Glasses as Anode Material for Rechargeable Zinc-Based Batteries. *Batteries* **2018**, *4* (1), 12.
(70) Stock, D.; Dongmo, S.; Damtew, D.; Stumpp, M.; Konovalova, A.; Henkensmeier, D.; Schlettwein, D.; Schröder, D. Design Strategy for Zinc Anodes with Enhanced Utilization and Retention: Electrodeposited Zinc Oxide on Carbon Mesh Protected by Ionomeric Layers. *ACS Appl. Energy Mater.* **2018**, *1*, 5579−5588.
(71) Kim, J.; Im, Y.; Park, K. S.; Cho, T. W.; Jeon, J.; Chung, K.; Kang, M. Improved Cell Performances in Ni/Zn Redox Batteries Fabricated by ZnO Materials with Various Morphologies Synthesized Using Amine Chelates. *J. Ind. Eng. Chem.* **2017**, *56*, 463−471.

NOTE ADDED AFTER ISSUE PUBLICATION

This article was initially published with an incorrect copyright statement and was corrected on or around May 5, 2021.

https://doi.org/10.1021/acsenergylett.0c02343
ACS Energy Lett. 2021, 6, 404−412